

The time-averaged magnetic field in numerical dynamos with non-uniform boundary heat flow

Peter Olson¹ and U. R. Christensen²

¹Department of Earth and Planetary Sciences, Johns Hopkins University, USA. E-mail: olson@jhu.edu

²Institut für Geophysik der Universität Göttingen, Germany

Accepted 2002 June 28. Received 2002 June 26; in original form 2001 November 14

SUMMARY

The time-averaged geomagnetic field on the core–mantle boundary is interpreted using numerical models of fluid dynamos driven by non-uniform heat flow. Dynamo calculations are made at Prandtl number $Pr = 1$, magnetic Prandtl numbers $Pm = 1$ – 2 , Ekman numbers $E = 3 \times 10^{-4}$ – 3×10^{-5} and Rayleigh numbers 10–30 times the critical value for different patterns of heat flow on the outer boundary of a rotating, electrically conducting spherical shell. The results are averaged over several magnetic diffusion times to delineate the steady-state magnetic field and fluid motion. When the boundary heat flow is uniform the time-averaged flow approaches axisymmetry and the magnetic field is mostly a geocentric axial dipole (GAD). The largest departure from GAD in this case is the octupole field component. When the amplitude of the boundary heat flow heterogeneity exceeds the average heat flow, the dynamos usually fail. Lesser amounts of boundary heterogeneity produce stable dynamos with time-averaged magnetic fields that depend on the form of the boundary heterogeneity. Elevated heat flow in the northern hemisphere produces a time-averaged axial quadrupole magnetic field comparable to the inferred paleomagnetic quadrupole. Azimuthally periodic boundary heat flow produces a time-averaged magnetic field component with the same azimuthal wavenumber, shifted in longitude relative to the heat flow pattern. Anomalously high and anomalously low magnetic flux density correlate with downwellings and upwellings, respectively, in the time-averaged fluid motion. A dynamo with boundary heat flow derived from lower-mantle seismic tomography produces anomalous magnetic flux patches at high latitudes and westward fluid velocity in one hemisphere, generally consistent with the present-day structure of the geodynamo.

Key words: dynamo models, Earth core dynamics, geodynamo, geomagnetic field, paleomagnetic field, thermal convection.

1 INTRODUCTION

One of the fundamental assumptions in paleomagnetism is that the main geomagnetic field approaches a specific reference state when averaged over sufficiently long times. The reference state most commonly used for the paleomagnetic field is a geocentric axial dipole, or GAD. Long-term departures from the reference GAD are particularly significant for the geodynamo, because they indicate influences on the core by the mantle. Here we use numerical dynamo models to investigate how heat flow heterogeneity on the core–mantle boundary influences the geodynamo and the time-averaged structure of the geomagnetic field.

Palaeomagnetic data from uniform polarity epochs (that is, away from times of polarity reversal or excursions), indicate two primary ways in which the geomagnetic field deviates from the GAD configuration in time average. First, there is evidence from palaeomagnetic inclinations from 0 to 5 Ma for a time-averaged axial quadrupole field component. Relative to the axial dipole, the amplitude of this

axial quadrupole is 0.04–0.05 (Merrill *et al.* 1996; Dormy *et al.* 2000). A persistent axial quadrupole term in the palaeomagnetic field, even a small one, is significant for the core, as it indicates that the geodynamo is not wholly symmetric about the equator in its long-term average behaviour. Secondly, there is a growing body of evidence from palaeomagnetic directions and intensities for deviations from axisymmetry in the 0–5 Ma palaeomagnetic field (Johnson & Constable 1995, 1997; Kelly & Gubbins 1997; Constable *et al.* 2000; Kono *et al.* 2000). Deviation from axisymmetry in the time-averaged palaeomagnetic field is also significant; it indicates that some effect breaks the rotational symmetry imposed on the geodynamo by the Earth's spin.

Because the timescale for magnetic field generation by motion in the fluid outer core is relatively short, of the order of 10^4 yr (Moffatt 1978), whereas the structure of the solid mantle changes on timescales of order 10^8 yr (Schubert *et al.* 2001), the long-term departures from GAD are generally thought to indicate some control of the geodynamo by lateral heterogeneity in the D'' region of the

lower mantle. There are several types of lateral heterogeneity in the D'' region that might plausibly influence the geodynamo, including anomalous topography at the core–mantle boundary, lateral heterogeneity in lower-mantle electrical conductivity, and lateral variations in heat flow at the core–mantle boundary. The effects of these on the geodynamo are usually referred to as topographic, electromagnetic and thermal coupling, respectively (Buffett 2000).

In this paper we investigate some consequences of thermal core–mantle coupling on the time-averaged structure of the geomagnetic field, using numerical dynamo models. We focus on one aspect of thermal coupling, the relationship of the pattern and amplitude of core–mantle boundary heat flow variations to the pattern and amplitude of the time-averaged departures from GAD in the geomagnetic field. We use high-resolution numerical dynamo models based on the full Navier–Stokes, magnetic induction and heat equations, without any *ad hoc* parametrizations, in order to delineate the physical relationships between the boundary heat flow variations, the time-averaged fluid motions within the core and the time-averaged structure of the dynamo.

2 CORE–MANTLE THERMAL COUPLING

The subject of thermal core–mantle coupling has a long history (Hide 1970; Vogt 1975; Jones 1977; Gubbins & Richards 1986; Gubbins & Bloxham 1987; Bloxham & Gubbins 1987; Bloxham & Jackson 1990; Gubbins 1997; Bloxham 2000a,b). Although many of the critical details are not yet understood, there is general agreement on the following basic mechanism. Because velocities of flow in the liquid outer core are far larger than in the solid mantle, the core and the mantle respond very differently to the continuity of heat flow and temperature at the core–mantle boundary. The lower mantle sees the outer core as a perfect fluid, and sees the core–mantle boundary as stress-free and isothermal. In contrast, the fluid outer core sees the mantle as solid and sees the core–mantle boundary as rigid with a prescribed heat flow. In this way, core–mantle thermal interaction is analogous to the thermal interaction between the ocean and the oceanic lithosphere. The lithosphere is sensitive to the ocean temperature at the sea floor, whereas the deep ocean is sensitive to heat flow variations imposed on it by the thermal structure of the lithosphere. In thermal core–mantle coupling the outer core plays a role similar to the ocean and the D''-layer at the base of the mantle plays a role similar to the lithosphere.

Considerations of heat transfer across the core–mantle boundary suggest that convection in the fluid outer core is influenced by the temperature structure of the lower mantle in two ways. First, the average thermal gradient at the base of the mantle governs the total heat flow from the core to the mantle. This, in turn, governs the cooling rate of the whole core, the rate of inner-core solidification, and the power available from convection to drive the geodynamo (Loper 1978; Lister & Buffett 1995; Labrosse *et al.* 1997). Secondly, convection in the core responds to lateral variations in lower-mantle thermal structure, particularly to variations in heat flow at the core–mantle boundary. Thermal convection in the core is enhanced where the core–mantle boundary heat flow is high and tends to be suppressed where the core–mantle boundary heat flow is low. In addition, a separate circulation system is produced within the outer core on the scale of the boundary heterogeneity.

Since core convection is the major energy source for the geodynamo, any long-term distortion of the convection pattern by non-uniform core–mantle boundary heat flow should affect the structure

of the time-averaged geomagnetic field. Accordingly, there should exist some relationship between the pattern of lower-mantle heterogeneity (as revealed by seismic tomography for example), the pattern of the time-averaged flow in the outer core, and the time-averaged structure of the geomagnetic field. Also, because the pattern of mantle heterogeneity evolves slowly, the coupling with the geomagnetic field should persist for millions of years and should be evident in the structure of the palaeomagnetic field.

The actual variations in heat flow on the core–mantle boundary can be inferred only very crudely, by assuming a certain relationship between seismic velocity variations and temperature variations in the lower mantle. The usual assumption is that lateral temperature variations in the lower mantle are anticorrelated with lateral variations in seismic velocity (Yuen *et al.* 1993). According to this assumption, those portions of the D''-layer with anomalously high seismic velocity (particularly high shear wave velocity) are relatively cold, and there the thermal gradient and the core–mantle boundary heat flow are relatively high. Conversely, where D''-layer seismic velocities are low the mantle is relatively hot, and there the thermal gradient and the core–mantle boundary heat flow are relatively low. This is the called the tomographic model of non-uniform core–mantle boundary heat flow. It has many shortcomings. For example, it ignores contributions to the seismic heterogeneity in the D''-layer from compositional variations, which could alter the relationship between shear wave velocity and heat flow. In addition, it does not constrain the amplitude of the non-uniform part of the core–mantle boundary heat flow. In spite of these shortcomings, tomographic heat flow has often been used as a thermal boundary condition for numerical models of core–mantle thermal coupling (Olson & Glatzmaier 1996; Glatzmaier *et al.* 1999; Gibbons & Gubbins 2000).

3 PREVIOUS NUMERICAL STUDIES OF CORE–MANTLE THERMAL COUPLING

The early numerical studies of core–mantle thermal coupling were aimed at finding the conditions necessary for locking the non-axisymmetric parts of the convection and magnetic field to the boundary heat flow heterogeneity pattern. Zhang & Gubbins (1992, 1993, 1996) showed that the azimuthal drift rate of the convection planform in a rotating sphere is affected by thermal heterogeneity on the boundary. For small-amplitude convection near the critical Rayleigh number, where the planform is azimuthally periodic, Zhang & Gubbins (1996) found steady states in which the azimuthal drift rate vanishes and the convection planform becomes stationary with respect to the boundary heterogeneity.

Gibbons & Gubbins (2000) used numerical models of finite amplitude rotating convection subject to spherical harmonic degree and order two boundary heat flux variations to determine the longitudinal phase relationship between the boundary heat flow and convection at higher Rayleigh numbers. At low rotation rates (relatively large Ekman number), they found the radial motion to be negatively correlated with the boundary heat flow. Downwellings occur beneath the high boundary heat flow sectors, where the fluid temperature is lowest. As the rotation rate is increased, they found the locked convection planform shifts progressively eastward, so that at the highest rotation rates considered (corresponding to an Ekman number $E = 10^{-4}$), the locked downwellings are located east of the high heat flow sectors, close to the longitude where the boundary heat flow anomaly is zero.

At higher Rayleigh numbers, rotating convection becomes chaotic, in addition to being intrinsically time dependent. In this

regime, thermal coupling occurs only in a statistical sense, as shown for rotating convection by Sun *et al.* (1994) and for rotating magnetoconvection by Olson & Glatzmaier (1996). The presence of a magnetic field and strong Lorentz forces further complicate the relationship between the convection pattern and the boundary heating. For this reason, numerical dynamo models are preferable to both rotating convection or rotating magnetoconvection for investigating core–mantle thermal coupling, because the dynamo models include the Lorentz force in a dynamically consistent way. A drawback of dynamo models is that they are more expensive to run, so fewer cases can be examined.

Sarson *et al.* (1997) examined the relationship between magnetic field, fluid velocity and boundary heating patterns using a so-called 2.5-dimensional numerical dynamo model, in which the azimuthal variation is restricted to wavenumbers $m = 0$ and 2. They find that the fluid motion and the magnetic field near the outer boundary are simply related: high magnetic flux density regions are located over the fluid downwellings, and low magnetic flux density regions are located over fluid upwellings. However, Sarson *et al.* (1997) also found that the relationship between the boundary heat flow pattern and the fluid motion is not so simple, and depends on the relative strength of the Lorentz and Coriolis forces, that is, on the Elsasser number Λ . For small Λ , rotation shifts the convection planform to the east of the boundary heat flow pattern, whereas at larger Λ the relationship is reversed, and the convection planform is shifted to the west of the boundary heat flow pattern.

The extreme truncation of azimuthal wavenumbers in 2.5-dimensional dynamo models limits their application to situations where the Rayleigh number of the convection is close to the critical value. Dynamo models with fully developed (highly supercritical) convection and low Ekman numbers show that the convection consists of narrow, quasi-geostrophic columns that are chaotically time dependent. In this regime it is unlikely that the entire dynamo would be locked to the boundary heat flow pattern. Instead, we expect that part of the magnetic field would be variable in time, so that the effects of the boundary heterogeneity would be seen best in long-term averages. Coe *et al.* (2000) analysed the time-averaged structure of some time-dependent dynamos with polarity reversals calculated by Glatzmaier *et al.* (1999). For a boundary heat flow pattern derived from lower-mantle seismic tomography, the dynamo model of Glatzmaier *et al.* (1999) shows a positive correlation between heat flow and the time-averaged non-dipole field: the non-dipole magnetic field on the outer boundary is most intense where the heat flow is highest (Coe *et al.* 2000). A qualitatively similar result has also been reported by Bloxham (2001), using a different time-dependent numerical dynamo model. Two explanations have been given for the correlation between high heat flow and high magnetic field intensity on the boundary. One is that the time-averaged (residual) fluid downwellings are located beneath high boundary heat flow regions, and concentrate the magnetic flux there. Another explanation is that the small-scale columnar convection is locally intensified beneath high boundary heat flow regions, and the intensified convection induces an anomalously strong magnetic field. Of course, it is possible that the two effects work together. The important point is that both of these mechanisms predict a close spatial relationship between the non-uniform boundary heat flow and the magnetic field intensity.

Dynamo models have also been used to interpret axisymmetric departures from GAD. Recently, Bloxham (2000b) obtained a strong axial octupole contribution to the time-averaged magnetic field by imposing a boundary heat flux pattern of spherical harmonic order two and degree zero. He also found that a pattern of spherical har-

monic degree and order two had little effect on the axisymmetric part of the magnetic field.

4 NUMERICAL MODEL

We use a modified version of the numerical dynamo model developed by G. A. Glatzmaier and described in Olson *et al.* (1999) and Christensen *et al.* (1999). We consider 3-D, time-dependent thermal convection in an electrically conducting, incompressible Boussinesq fluid in a rotating spherical shell. The governing equations are: (1) the Navier–Stokes equation with full inertia, Coriolis, and Lorentz forces, using constant Newtonian viscosity; (2) the heat transport equation for the temperature; (3) the induction equation for the magnetic field. The spherical shell has the same ratio of inner radius r_i to outer radius r_o as the Earth's outer core, $r_i/r_o = 0.35$. Both spherical boundaries are assumed to be rigid, impermeable and electrically insulating. The electrically insulating outer boundary condition is a justifiable approximation for the core–mantle boundary, since the mantle is much less conducting than the core. Our assumption of an electrically insulating inner boundary condition is a matter of numerical convenience. It is not *a priori* justifiable for the inner-core boundary, because the electrical conductivity of the solid inner core is expected to be comparable to the fluid outer core (Secco & Schloessin 1989). However, in a separate study using this model, Wicht (2002) finds only minor differences in the behaviour of dynamos with electrically conducting versus insulating inner-core boundaries. In particular, he finds very small differences in the time-averaged fields with and without inner-core conductivity. Since we consider dynamos in the same general parameter range as Wicht, we are confident that our interpretations of the time-averaged states in this study apply equally to models with the same parameters but with conducting inner cores. In this study we examine numerical dynamos in the fully developed regime of Olson *et al.* (1999). These dynamos are dominated by stable, non-reversing, nearly axial dipole magnetic fields, and produce well-defined time-averaged states. Magnetic reversals have been obtained with the model we use here, but at significantly larger Rayleigh numbers, where the dipole field is more time variable (Kutzner & Christensen 2002).

The thermal boundary conditions we use are as follows. The inner boundary is isothermal, with a prescribed uniform temperature. The outer boundary has prescribed heat flow. The local heat flux on the outer boundary q is the sum of a surface average q_o plus a spatially variable part $q'(\theta, \phi)$ representing the boundary heterogeneity. We define the heterogeneity amplitude q^* as half the ratio of the peak-to-peak boundary heat flow heterogeneity to the average; that is,

$$q^* = \frac{q'_{\max} - q'_{\min}}{2q_o}. \quad (1)$$

The results of calculations using several different spatial patterns of the boundary heat flow heterogeneity are compared. These include uniform heating ($q^* = 0$), patterns consisting of individual spherical harmonics $q' \sim Y_l^m$, and a tomographic pattern derived by assuming $-q'$ has the same pattern as the first four spherical harmonic degrees in the model of lower-mantle seismic shear wave heterogeneity by Masters *et al.* (1996). We refer to these different cases as uniform Y_{lm} and tomographic, respectively.

In addition to the boundary heterogeneity amplitude, the other dimensionless input parameters are the Rayleigh number Ra , the Ekman number E , the Prandtl number Pr and the magnetic Prandtl number Pm . The lower the Ekman number, the higher the spatial

Table 1. Dynamo model parameters.

Input parameter	Definition	Range
Prandtl number	$Pr = \nu/\kappa$	1
Magnetic Prandtl number	$Pm = \nu/\lambda$	1–2
Ekman number	$E = \nu/\Omega D^2$	$0.3\text{--}3 \times 10^{-4}$
Rayleigh number	$Ra = \alpha g_0 q_0 D^4 / k \kappa \nu$	$2.5 \times 10^6\text{--}2 \times 10^8$
Boundary heterogeneity	$q^* = (q'_{\max} - q'_{\min})/2q_0$	–0.5 to +1.25
Output parameter	Definition	Outer core
Magnetic Reynolds number	$Re = uD/\lambda$	500
Elsasser number	$\Lambda = \sigma B^2 / \rho \Omega$	~ 1
Gauss ratios	$(Glm, Hlm) = (g_l^m, h_l^m)/g_1^0$	–0.1 to +0.1

Notes: $D = r_o - r_i$ shell thickness; ν, κ, λ viscous, thermal, magnetic diffusivities; k thermal conductivity; σ electrical conductivity; α thermal expansivity; g_0 outer boundary gravity; ρ average density; Ω rotation angular velocity; q_0, q' mean, variable boundary heat flows; u fluid velocity; B magnetic induction; g_l^m time-averaged magnetic field Gauss coefficients.

and temporal resolution that is required. In our calculations we truncate at spherical harmonic degree $l_{\max} = 53$ at $E = 3 \times 10^{-4}$ and $l_{\max} = 106$ at $E = 3 \times 10^{-5}$. These spherical harmonic truncations were chosen on the basis of spectral resolution tests by Christensen *et al.* 1999 at $E = 1 \times 10^{-4}$. As shown in Fig. 10 (in Section 5), the time-averaged magnetic field spectra decrease by at least a factor of 10^3 over this spectral range. Our lowest Ekman number is several orders of magnitude too large for the core, even if a turbulent viscosity is assumed, so the viscosity and thermal diffusivity are more important in our calculations than in the core.

Two important output parameters are the volume-averaged Elsasser number Λ , a measure of the dynamo magnetic field strength, and the volume-averaged magnetic Reynolds number Rm , a measure of the fluid velocity in the dynamo. To characterize the departures of the time-averaged magnetic field from the reference GAD, we follow the convention used in palaeomagnetism (Merrill *et al.* 1996), in which magnetic field anomalies are described using ratios of individual Gauss coefficients g_l^m or h_l^m to the Gauss coefficient of the axial dipole magnetic field g_1^0 . We refer to these as Gauss ratios, Glm or Hlm , respectively. The definitions of the dimensionless parameters in terms of physical quantities are given in Table 1. Table 2 gives the notation of all the variables we use in analysing the calculations, the fundamental scaling for the basic variables and the numerical values of the scalefactors we use for converting our results to dimensional form.

The calculations are started from dynamo solutions that were obtained previously using isothermal boundary conditions but otherwise with comparable parameters (Christensen *et al.* 1999). When thermal equilibrium is reached, as indicated by statistically steady

flow, the outer boundary condition is changed from the prescribed temperature to the prescribed heat flow. Each calculation is then continued beyond its initial transient response to the new boundary condition, until an approximate global equilibration is reached, where the time-series of total magnetic and kinetic appear to be statistically stationary. We then continue the calculation and compute running time averages of the temperature, velocity and magnetic fields. These time averages provide the basic data for our analysis. We stop the calculation at an averaging time t^* when the change in the time-averaged radial magnetic field at the outer boundary B_r becomes sufficiently small. As used here, the term ‘sufficiently small’ is somewhat arbitrary. We have adopted a practical definition, in which a calculation is stopped when the large-scale pattern of B_r on the outer boundary has stabilized. The averaging times shown in Table 2 are given in magnetic diffusion time units, based on the fluid shell thickness. In terms of our scaling, one magnetic diffusion time is very nearly equal to four dipole diffusion times. Assuming an electrical conductivity of $\sigma = 6 \times 10^5 \text{ S m}^{-1}$ (Secco & Schloessin 1989) for example, one magnetic diffusion time unit corresponds to approximately 122 000 yr in the core.

Finally, we point out that all of the dynamo solutions shown in this paper have magnetic fields dominated by a dipole component with ‘reversed’ polarity, that is, a polarity opposite to the present-day geomagnetic field. The reverse dipole polarity is a result of the initial conditions we use, and otherwise has no effect on our interpretations.

5 RESULTS

Table 3 gives the input parameters for all the calculations in terms of the notation from the previous section. Table 3 also summarizes some of the important results for each case, including the Elsasser and magnetic Reynolds numbers, the time-averaged kinetic and magnetic energies (as defined in Olson *et al.* 1999), and the Gauss coefficient of the axial dipole part of the time-averaged magnetic field, g_1^0 .

Most of the calculations we analyse are made at $Ra = 2.5 \times 10^6$ and $E = 3 \times 10^{-4}$. As shown in Table 3, the magnetic energy exceeds the kinetic energy in these cases, although not by as much as it probably does in the core. Table 3 also shows the volume-averaged magnetic Reynolds and Elsasser numbers are about 145 and 5, respectively, in these dynamos. These are broadly in the range of the geodynamo, although they are slightly low and slightly high, respectively, compared with typical estimates from the present-day geomagnetic field. Similarly, the Gauss coefficients of the axial dipole g_1^0 are typically 60 per cent higher than the present-day geomagnetic field. For comparison purposes we have also included two additional cases of the Y_{22} boundary heating pattern at higher Rayleigh number and lower Ekman number, respectively.

Fig. 1 shows the structure of the dynamo with uniform boundary heating averaged over $t^* = 6.7$ magnetic diffusion times, equivalent to about 800 000 yr in the core. The flow pattern in Figs 1(a) and (b) is taken close to the boundary but below the viscous Ekman layer. The time-averaged magnetic field and fluid motion are nearly axisymmetric and nearly antisymmetric about the equator. The small departures from true axisymmetry seen in the figure are tending toward zero with increasing averaging time. The time-averaged magnetic field in Fig. 1(c) is clearly dominated by the GAD component. The most noticeable departure from GAD is seen at high latitudes in both hemispheres, and consists of a low-intensity field directly over the poles, the polar cap minima and rings of high-intensity

Table 2. Scaling.

Notation	Variable	Scale factor	Value
θ, ϕ	Colatitude, east longitude	—	—
r	Radius	D	2260 km
t^*	Averaging time	D^2/λ	122 000 yr
B_r	Radial magnetic field at r_o	$\sqrt{\rho \Omega / \sigma}$	1.16 mT
u_r	Radial velocity near r_o	λ/D	$5.87 \times 10^{-7} \text{ m s}^{-1}$
ψ	Toroidal streamfunction near r_o	λ	$1.33 \text{ m}^2 \text{ s}^{-1}$
T_o	Temperature at r_o	Dq_0/k	—

Table 3. Summary of results.

Pattern	q^*	Ra	E	Pm	E_{kin}	E_{mag}	Rm	Λ	t^*	g_1^0 (nT)
Uniform	0	2.5×10^6	3×10^{-4}	2	2540	4280	143	5.1	6.7	57 620
Y_{22}	0.3125	2.5×10^6	3×10^{-4}	2	2580	4140	144	5.0	9.3	55 643
Y_{22}	0.625	2.5×10^6	3×10^{-4}	2	2700	3730	147	4.5	12	50 500
Y_{22}	1.25	2.5×10^6	3×10^{-4}	2	Failed	Failed	na	na	na	na
Y_{22}	0.5	2.8×10^7	1×10^{-4}	2	13 500	27 500	329	11	3.3	73 756
Y_{22}	0.5	2.0×10^8	3×10^{-5}	1	35 400	15 100	266	9.1	1.0	81 300
Y_{10}	0.5	2.5×10^6	3×10^{-4}	2	2590	4450	144	5.3	6.9	57 962
Y_{11}	0.5	2.5×10^6	3×10^{-4}	2	2750	4030	148	4.8	8.6	49 765
Y_{20}	0.5	2.5×10^6	3×10^{-4}	2	2630	4670	145	5.6	5.3	48 989
Y_{20}	1.0	2.5×10^6	3×10^{-4}	2	Failed	Failed	na	na	na	na
Y_{20}	-0.5	2.5×10^6	3×10^{-4}	2	2700	3560	147	4.3	5.3	56 766
Tomographic	0.5	2.5×10^6	3×10^{-4}	2	2600	4270	144	5.1	7.2	53 014

field at the latitude of the inner-core tangent cylinder, the tangent cylinder maxima. As indicated by the time-averaged radial velocity pattern, the two polar cap minima result from magnetic flux divergence by upwelling polar plumes, and the tangent cylinder maxima result from magnetic flux concentration by surface convergence and downwelling along the tangent cylinder.

It is customary to describe the departures from GAD in the time-averaged magnetic field in terms of specific Gauss ratios. As shown in Fig. 2, the quadrupole ratio for the uniform boundary heat flow case is $G_{20} = 0.001$, indicating very little difference between the northern and southern hemisphere fields. In contrast, the axial octupole ratio is $G_{30} = 0.061$, and is by far the largest departure from GAD in this case. The size of the ‘flux lobe anomaly’ is indicated by the following Gauss ratios: $G_{31} = 0.002$, $H_{31} = 0$ and $G_{32} = -0.002$ and $H_{32} = 0$. These non-axial coefficients are very small and are tending toward zero with increasing averaging time as the magnetic field approaches axisymmetry.

We have examined the response of model dynamos to various amounts of spherical harmonic degree two and order two boundary heat flow heterogeneity. The Y_{22} heat flow pattern has been used in previous studies as a simplified representation of the core–mantle boundary heat flow heterogeneity (Sarson *et al.* 1997; Glatzmaier *et al.* 1999; Gibbons & Gubbins 2000) because of its similarity to the long-wavelength seismic structure of the lower mantle, which contains a large signal at this harmonic (Masters *et al.* 1996).

As indicated by the results in Table 3, very large amplitude heterogeneity tends to kill dynamo action, for both the Y_{20} and Y_{22} heat flow patterns. This behaviour is consistent with the results of magnetoconvection calculations by Olson & Glatzmaier (1996), who found that large lateral heterogeneity in boundary heating destroys the columnar convection and destabilizes the dipole field. When the amplitude of the heat flow heterogeneity exceeds the average boundary heat flow, that is, when q^* exceeds one, stable thermal stratification forms beneath regions where the boundary heat flow is low. This tends to segment the fluid into convecting regions separated by non-convecting regions, and creates strong thermal winds that are ill-suited to maintaining a stable GAD-type dynamo.

Fig. 3 shows instantaneous dynamo structure for the Y_{22} boundary heat flow with amplitude 0.625. The instantaneous flow is dominated by elongated convection columns, and the instantaneous magnetic field is concentrated in high-intensity flux patches with dimensions comparable to the cross-section of the convection columns. Comparison of Figs 3(a) and (c) shows that the high-intensity magnetic

flux patches correlate with cyclonic vortices in which the radial flow near the outer boundary is downward. These flux patches are formed within and are concentrated by fluid downwellings in the cores of the cyclones. Individual flux patches are transient, but the summation of the magnetic fields from all the patches produces the net GAD. We see evidence in a series of snapshots for a modulation of the convection by the boundary heat flow, particularly at low latitudes. Statistically, the most intense low-latitude convection occurs in the longitude sectors with high boundary heat flow. This particular modulation has most effect at low latitudes where the time-averaged radial magnetic field is weak. At high latitudes where the radial field is most intense, the modulation occurs by a different mechanism.

Figs 4 and 5 show the structure of the same model with Y_{22} heating, averaged over $t^* = 12$ diffusion times, equivalent to about 1.5 Myr in the core. The time-averaged magnetic field and fluid motion both have clearly defined structure at azimuthal wavenumber $m = 2$. As seen in the streamfunction pattern, the time-averaged toroidal flow in each hemisphere consists of two parts: a polar vortex inside the inner-core tangent cylinder (which intersects the outer surface at 69° latitude), and an $m = 2$ columnar flow outside the tangent cylinder attributed the boundary heat flow heterogeneity. As shown in Fig. 5, the vorticity reverses sign between the pole and the inner-core tangent cylinder, so that the surface integral of the polar vortices is nearly zero. This shields the fluid outside the tangent cylinder from the vortex circulation inside; in effect, the two regions are isolated from each other. The amplitude of the residual toroidal flow corresponds to a magnetic Reynolds number of about 15, which is smaller than (but not insignificant in comparison with) the $Rm \simeq 100$ for the instantaneous flow in the snapshot shown in Fig. 3.

The locations of the columnar vortices in the time-averaged flow are controlled by the boundary heat flow pattern. In the $E = 3 \times 10^{-4}$ case, equatorial downwellings occur in the high boundary heat flow sectors, as shown in Fig. 4. In detail, the equatorial downwellings are shifted slightly eastward relative to the heat flow maxima. Each equatorial downwelling generates an axially cyclonic convection column to its west and an axially anticyclonic column located to its east. Since the axial flow in cyclonic columns is downwelling near the outer boundary, these structures tend to accumulate magnetic flux, whereas the near-surface upwellings in the anticyclonic columns tend to expel magnetic flux. If the residual flow consisted of azimuthally periodic $m = 2$ columns only, the high-intensity magnetic flux patches would be located directly over the cyclonic columns. Instead, Fig. 4 shows that the anticyclones are

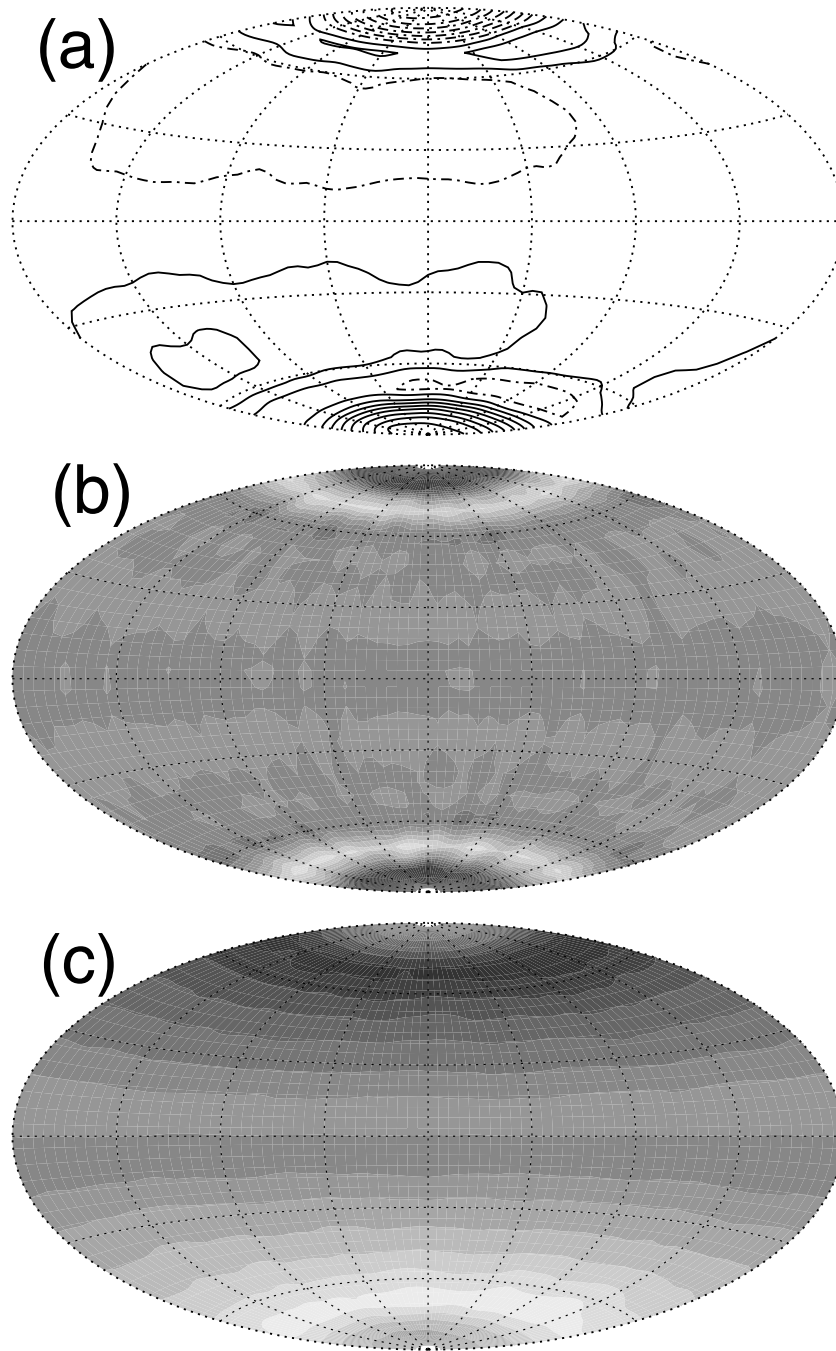


Figure 1. Time-averaged dynamo with uniform boundary heat flow. (a) Toroidal streamlines at depth $r_0 - r = 0.04$, contour interval 1; (b) radial velocity at depth $r_0 - r = 0.04$, contour interval 0.8; (c) radial magnetic field at r_0 , contour interval 0.16. Dark = positive, light = negative.

slightly stronger than the cyclones, and in addition, there is also magnetic flux concentration by the axisymmetric downwelling along the tangent cylinder. The effect of this combination of flows is to displace the magnetic flux patches poleward and eastward from the cyclone centres.

The specific relationship between the magnetic flux patches and the residual circulation can be understood in terms of a balance between magnetic field line stretching by downwellings and upwellings versus magnetic diffusion. At high latitudes, the dominant component of magnetic diffusion is tangential, that is, diffusion over the spherical surface. The balance of these terms in the time-averaged

magnetic induction equation for the radial component of the magnetic field near the outer boundary r_0 gives

$$B_r u_r \simeq (r_0 - r) \nabla_H^2 B_r, \quad (2)$$

where B_r and u_r are time averages of the dimensionless radial magnetic field and radial fluid velocity, respectively. According to eq. (2), the anomalously low-intensity flux patches (for example, patches in the northern hemisphere where $\nabla_H^2 B_r$ is large and positive) are related to the fluid upwellings ($u_r > 0$), and anomalously high-intensity flux patches are related to fluid downwellings

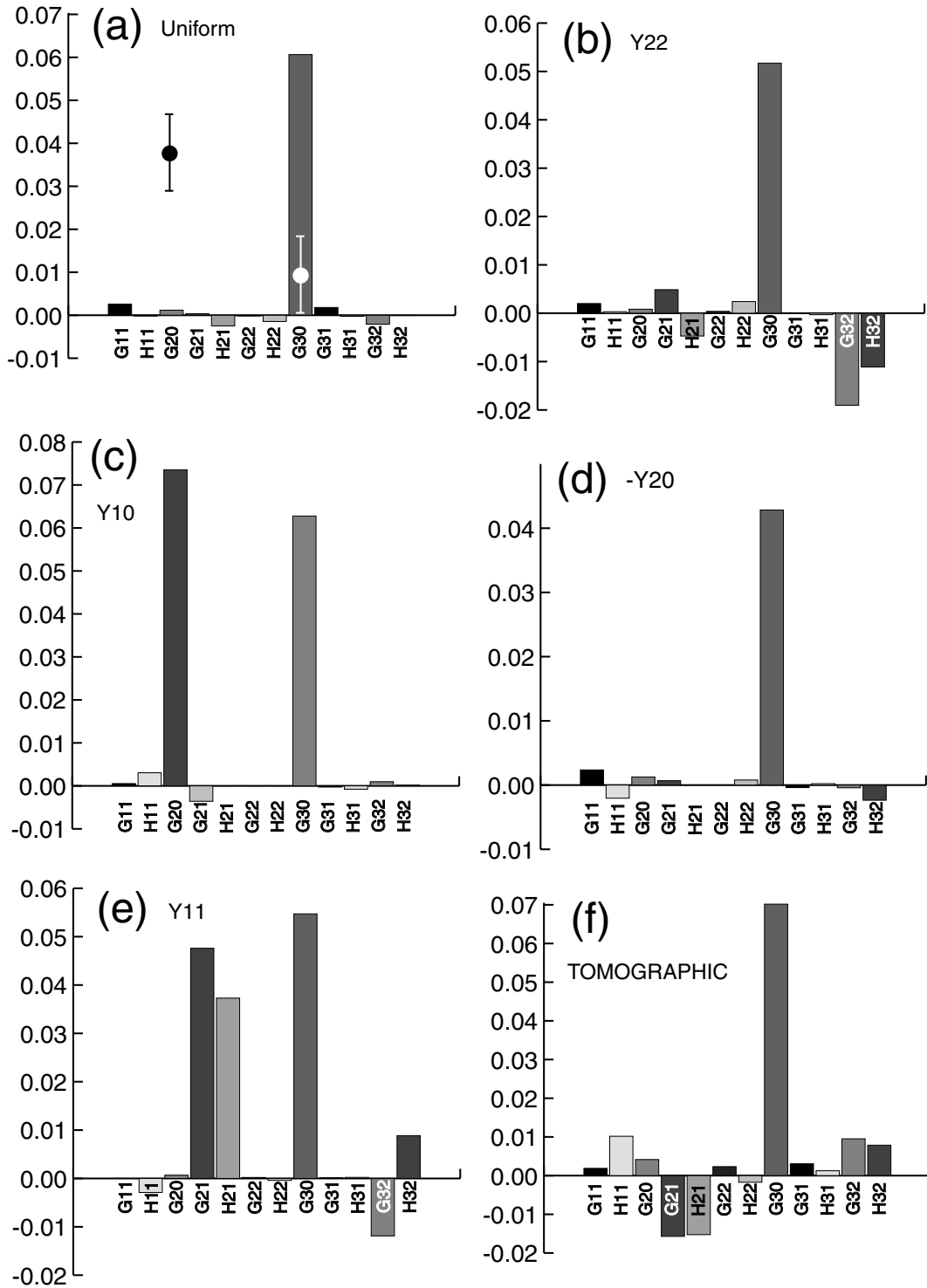


Figure 2. Ratios of Gauss coefficients normalized by the GAD term g_1^0 from the time-averaged magnetic fields of six cases with different boundary heat flow patterns in Table 3. (a) Uniform; (b) Y_{22} , $q^* = 0.625$; (c) Y_{10} , $q^* = 0.5$; (d) Y_{20} , $q^* = 0.5$; (e) Y_{11} , $q^* = 0.5$; (f) tomographic, $q^* = 0.5$. The error bars indicate the range of palaeomagnetic estimates of the ratios G_{20} and G_{30} .

($u_r < 0$). The relationship implied by (2) can be seen by comparing Figs 5(b) and (d), which shows the close similarity between u_r and $\nabla_H^2 B_r$ over the northern hemisphere of the dynamo model.

A linear relationship between the amplitude of the anomalous magnetic field and the amplitude of the boundary heat flow hetero-

geneity can be seen from the results of calculations with the same heat flow pattern but different amplitudes. Fig. 2 shows the Gauss ratios G_3^2 and H_3^2 used to characterize the magnetic flux patches produced by the Y_{22} boundary heat flow variation with $q^* = 0.625$. Comparing these ratios with the same ratios from the other Y_{22} -type

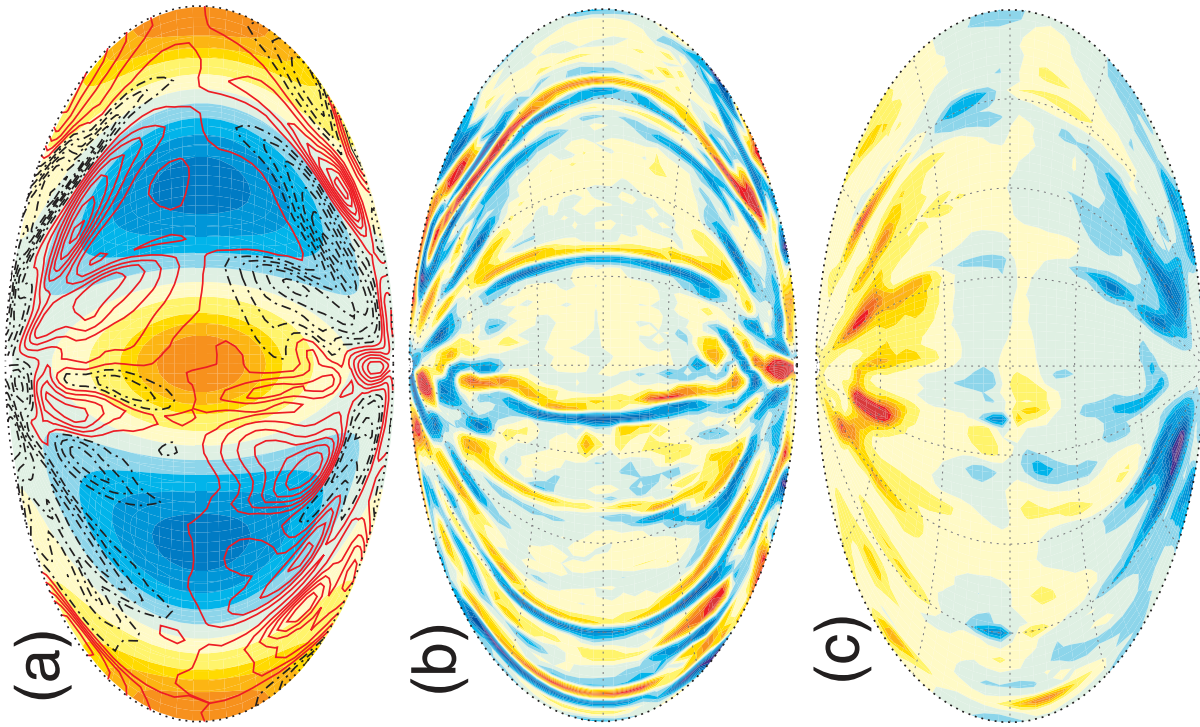


Figure 3. Snapshots of dynamo with Y_{22} boundary heat flow pattern, $q^* = 0.625$, $E = 3 \times 10^{-4}$. (a) Toroidal streamlines at $r_0 - r = 0.04$, contour interval 3, over boundary heat flow heterogeneity; (b) radial velocity at depth $r_0 - r = 0.04$, contour interval 4; (c) radial magnetic field at r_0 , contour interval 0.4. Red = positive, blue = negative.

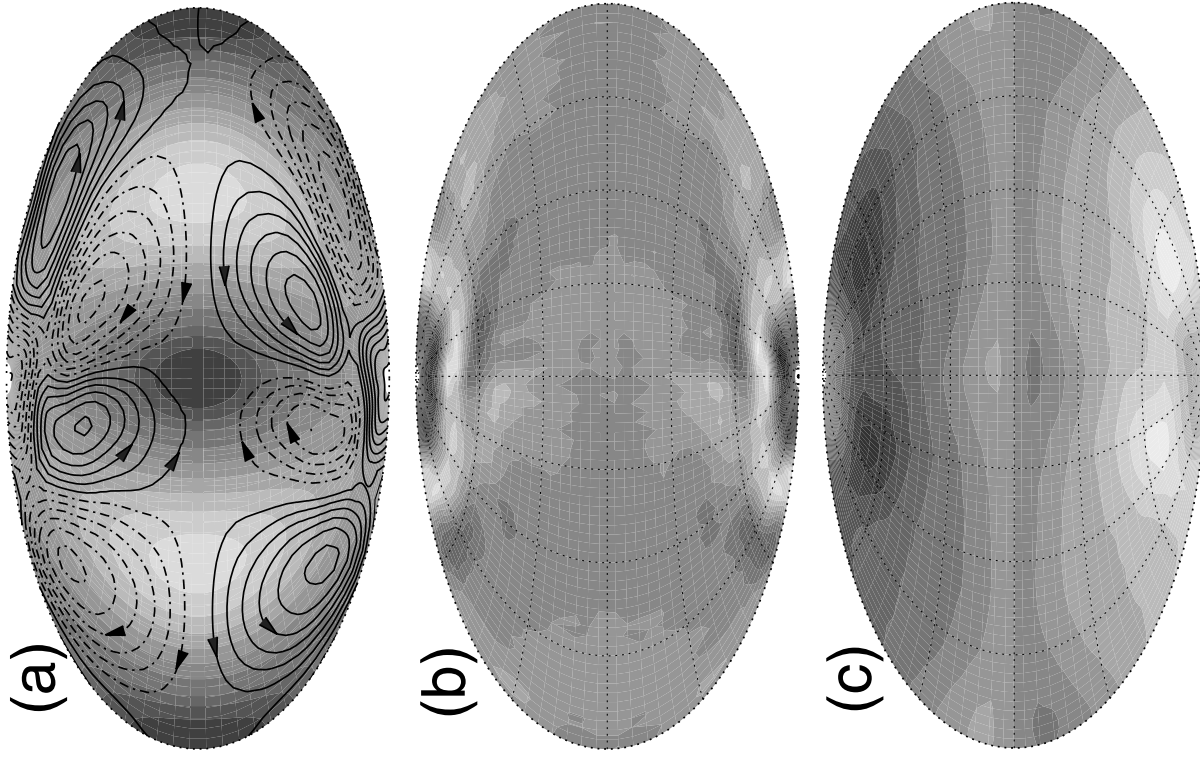


Figure 4. Time-averaged dynamo with Y_{22} boundary heat flow pattern, $q^* = 0.625$, $E = 3 \times 10^{-4}$. (a) Toroidal streamlines (with velocity direction arrows) at depth $r_0 - r = 0.04$, contour interval 1.0, over boundary heat flow heterogeneity; (b) radial velocity at depth $r_0 - r = 0.04$, contour interval 0.8; (c) radial magnetic field at r_0 , contour interval 0.16. Dark = positive, light = negative.

cases in Table 3 indicates that the amplitudes of $G32$ and $H32$ are directly proportional to the non-uniform heat flow amplitude q^* .

Most of our conclusions are drawn from cases with Ekman number $E = 3 \times 10^{-4}$. This Ekman number allows for calculations with a long averaging time t^* and provides well-defined time-averaged flow and magnetic field structures. For comparison, we have also examined dynamos with the same Y_{22} boundary heat flow pattern but lower Ekman number, specifically $E = 1 \times 10^{-4}$ and 3×10^{-5} . Some of the global properties of the time-averaged results of these cases are given in Table 3. The cases with lower Ekman number have shorter averaging times. However, the same basic structures in the time-averaged magnetic field seen in Figs 4 and 5 are also present in the lower Ekman number cases. One significant difference is that the azimuthal phase shift between the time-averaged magnetic field and the boundary heating pattern changes with Ekman number. Fig. 6 indicates that the westward shift of the magnetic field relative to the boundary heating decreases with decreasing Ekman number. The same trend is found for the radial fluid velocity. It is possible that the phase shift vanishes or even changes sign at lower Ekman numbers, but we have not been able to verify this with our model, owing to the extraordinarily high spatial resolution needed for such a calculation. Finally, we note that, even though the intensity of the anomalous flux patches increases with the boundary heat flow anomaly q^* , their locations and shapes are insensitive to this parameter.

The cases with Y_{22} -type heating show that the locations of anomalous magnetic flux patches are controlled by the residual circulation and do not necessarily correspond to the longitudes of maximum boundary heating. The same general result is found in all of the dynamo models in this study. It can be seen particularly well in the case of Y_{11} -type boundary heat flow shown in Fig. 7. Here a single high-intensity flux patch forms in each hemisphere. In this case the $m = 1$ residual circulation consists of two columnar cells that are spiral shaped in cross-section with a pronounced prograde tilt, similar to what has been seen in laboratory experiments (Sumita & Olson 1999). The spiral shape shifts the centre of the cyclonic cell so far to the west that the high-intensity flux patches lie in the low heat flow hemisphere, not in the high one.

North–south hemispheric asymmetry is another type of boundary heterogeneity that may be important for the geodynamo. As discussed in the introduction, the palaeomagnetic field appears to have a persistent axial quadrupole part, which might be caused by differences in heat flow between the northern and southern hemispheres of the core–mantle boundary. We have examined the response of a dynamo model to north–south hemisphere differences in boundary heat flow. Fig. 8 shows meridional cross-sections of the dynamo structure with a Y_{10} (i.e. $\cos \theta$) boundary heat flow pattern and amplitude $q^* = 0.5$. In this case the average heat flow in the northern hemisphere is 50 per cent above its average in the southern hemisphere. The meridional sections in Fig. 8 are averages, both in azimuth and over a time $t^* = 4.6$. The effect of elevated heat flow in the northern hemisphere is to enhance the convection and the meridional circulation there, which tends to concentrate the poloidal magnetic flux in the northern hemisphere and remove it from the southern hemisphere. The Gauss ratios in Fig. 2 clearly show the sensitivity to north–south heat flow differences. The quadrupole ratio in this case is $G20 = 0.07$, significantly larger than any of our cases without a north–south heat flow difference. For comparison, the quadrupole ratio we obtain in this case is larger than the quadrupole ratio inferred for the 0–5 Ma palaeomagnetic field (Merrill *et al.* 1996; Dormy *et al.* 2000). This calculation indicates that a relatively small north–south difference in heat flow can support time-averaged quadrupole

magnetic fields comparable to those inferred from palaeomagnetic inclinations.

All of the dynamos in this study contain large axial octupole components in their time-averaged magnetic fields, with positive $G30$ -ratios. The octupole components can be seen in the Gauss ratio spectra in Fig. 2, and also in the maps of time-averaged radial magnetic field, where the presence of the octupole field causes the intensity of the radial magnetic field at low latitudes to be less than for a purely axial dipolar field. The Gauss ratio of the axial octupole $G30$ is typically 0.06 or greater for most of the cases in Table 3. This is substantially larger than the 0.01 ± 0.01 range inferred for $G30$ by Merrill *et al.* (1996) for the 0–5 Ma palaeomagnetic field. However, we note that there is evidence from statistical analyses of globally distributed palaeoinclinations for a strong axial octupole contribution prior to 250 Ma, with $G30$ -values up to +0.25 (Kent & Smethurst 1998; Bloxham 2000b). There is also evidence from northern hemisphere palaeolatitudes for a relatively strong octupole during 300–40 Ma, with $G30 \simeq 0.1$ (Van der Voo & Torsvik 2001). So perhaps the departure from GAD in our dynamo models is more typical of the ancient palaeomagnetic field.

We have investigated the sensitivity of $G30$ to different axisymmetric patterns of boundary heat flow heterogeneity, including positive and negative Y_{20} -variations. As shown in Fig. 2 and Table 3, negative Y_{20} heat flow variations (with elevated heat flow at the equator relative to both poles) reduces $G30$, whereas a positive Y_{20} boundary heat flow actually increases $G30$ above the values shown for the other cases in Fig. 2. Unfortunately $G30$ is not very sensitive to this type of boundary heat flow, and probably a very large negative Y_{20} contribution to core–mantle boundary heat flow would be required to entirely suppress this ratio in the time-averaged magnetic field.

The calculations described so far have periodic boundary heat flow variations proportional to a single spherical harmonic. These cases show it is possible to account for the axial quadrupole departure from GAD with a small amount of Y_{10} boundary heating, and the flux lobe departures from GAD with Y_{22} boundary heating. However, these same cases contain an axial octupole that is significantly larger than inferred for the 0–5 Ma palaeomagnetic field. To reduce the axial octupole, additional zonal harmonics must be added to the boundary heat flow pattern. In principle, it would seem possible to construct an *ad hoc* boundary heat flow spectrum consisting of a sum of spherical harmonic contributions, which would produce a time-averaged magnetic field consistent with all of the palaeomagnetic constraints.

An alternative approach is to assume that the heat flow spectrum on the core–mantle boundary is similar to the spectrum of lower-mantle heterogeneity imaged by seismic tomography, and calculate the resulting time-averaged magnetic field. Fig. 9 shows the dynamo structure with a boundary heat flow pattern proportional to the lower-mantle seismic shear wave model of Masters *et al.* (1996), truncated at spherical harmonic degree and order $l, m = 4$, with amplitude $q^* = 0.5$. For this case the averaging time is $t^* = 7.2$, equivalent to about 0.9 Myr in the core. The Gauss ratios from this case are shown in Fig. 2.

The tomographic heat flow pattern generates a time-averaged magnetic field that includes all of the components found in the periodic cases discussed above. In particular, the magnetic field in Fig. 9 includes the polar minimum and tangent cylinder maximum, plus high-intensity flux patches in each hemisphere. It also includes significant departures from symmetry with respect to the equator. There are two unequal flux patches in the northern hemisphere, and only one in the southern hemisphere. In addition, the longitude of the lone

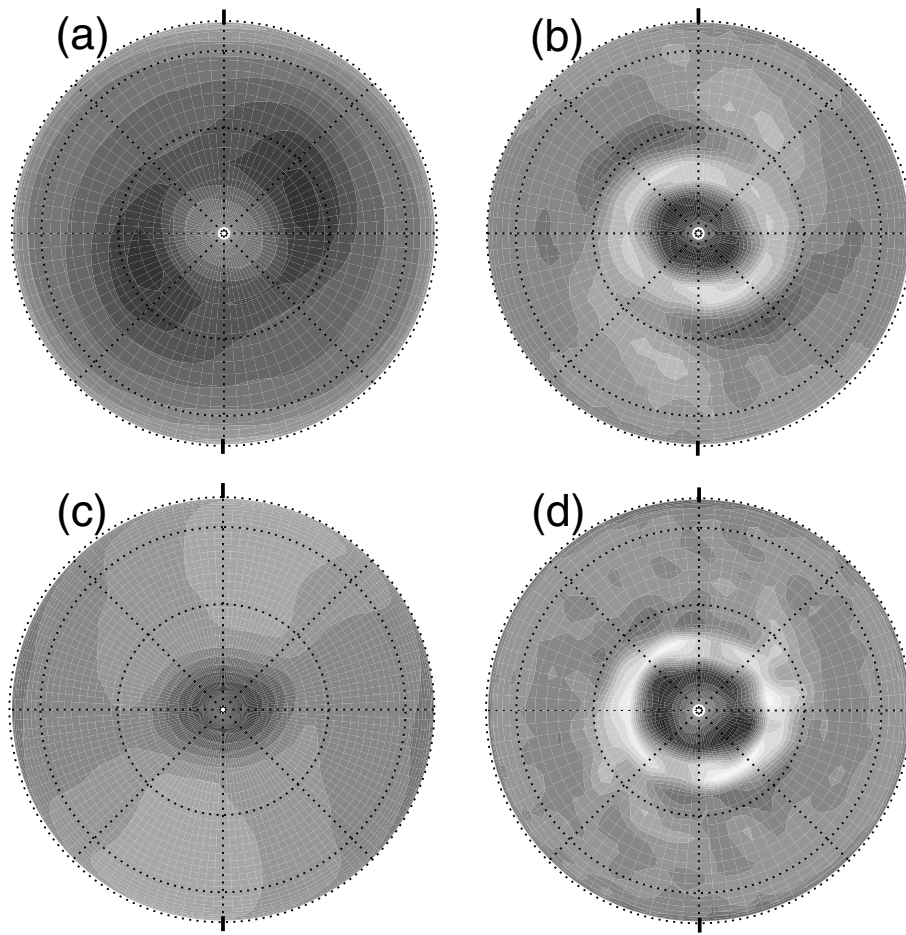


Figure 5. North polar views of time-averaged dynamo with Y_{22} boundary heat flow pattern, $q^* = 0.625$, $E = 3 \times 10^{-4}$. Tick marks indicate longitudes with maximum boundary heat flow. (a) Radial magnetic field at r_o , contour interval 0.16; (b) radial velocity at depth $r_o - r = 0.04$, contour interval 0.8; (c) temperature at r_o , contour interval is 1/17 of the mean temperature contrast between inner and outer boundary; (d) $\nabla_H^2 B_r$ at r_o . Dark = positive, light = negative.

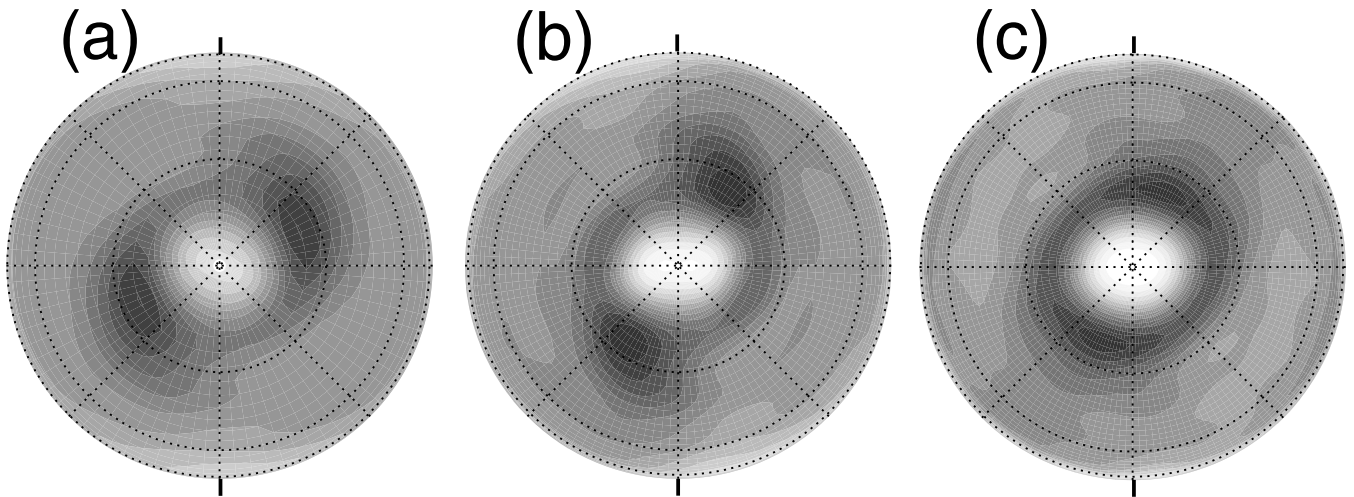


Figure 6. North polar views of filtered time-averaged radial magnetic fields at r_o from dynamos with Y_{22} boundary heat flow pattern at various Ekman numbers. The filtering removes the axial dipole term, and all terms with odd m and even l , in order to enhance the flux patches. Tick marks indicate longitudes with maximum boundary heat flow. (a) $E = 3 \times 10^{-4}$; (b) $E = 1 \times 10^{-4}$; (c) $E = 3 \times 10^{-5}$. Dark = positive, light = negative.

southern hemisphere patch differs slightly from the longitude of the largest one in the northern hemisphere. The time-averaged magnetic field produced by the tomographic boundary heat flow is similar in these respects to the time average of the historical geomagnetic field

on the core–mantle boundary (Blokhin & Jackson 1992). It also has points of similarity with some models of the 0–5 Ma time-averaged palaeomagnetic field (Johnson & Constable 1995; Kelly & Gubbins 1997).

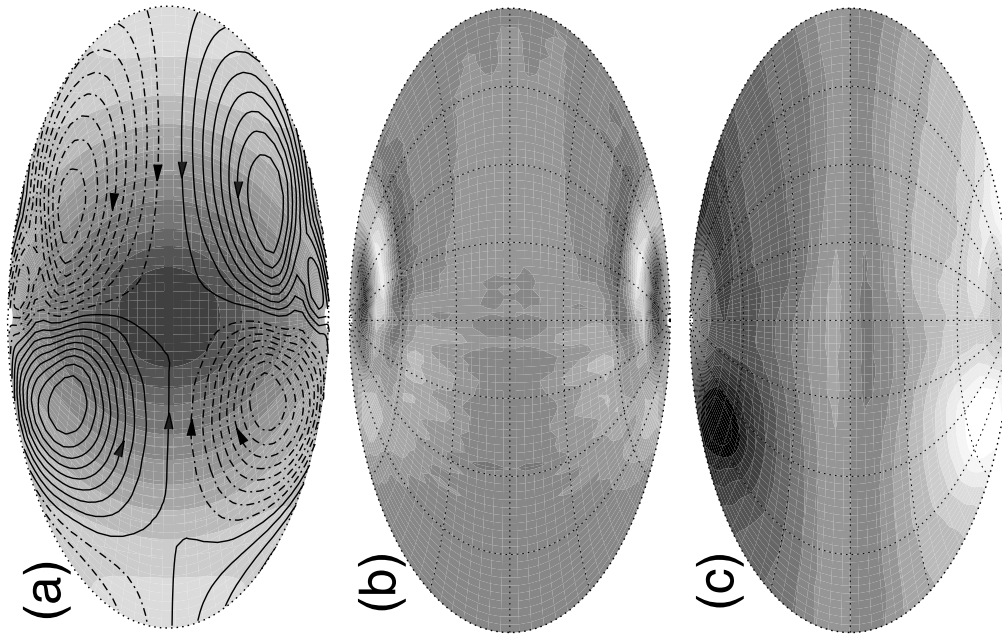


Figure 7. Time-averaged dynamo with Y_{11} boundary heat flow pattern, $q^* = 0.5$, $E = 3 \times 10^{-4}$. (a) Toroidal streamlines at $r_0 - r = 0.04$, contour interval 1, over boundary heat flow heterogeneity; (b) radial velocity at depth $r_0 - r = 0.04$, contour interval 0.8; (c) radial magnetic field at r_0 , contour interval 0.12. Dark = positive, light = negative.

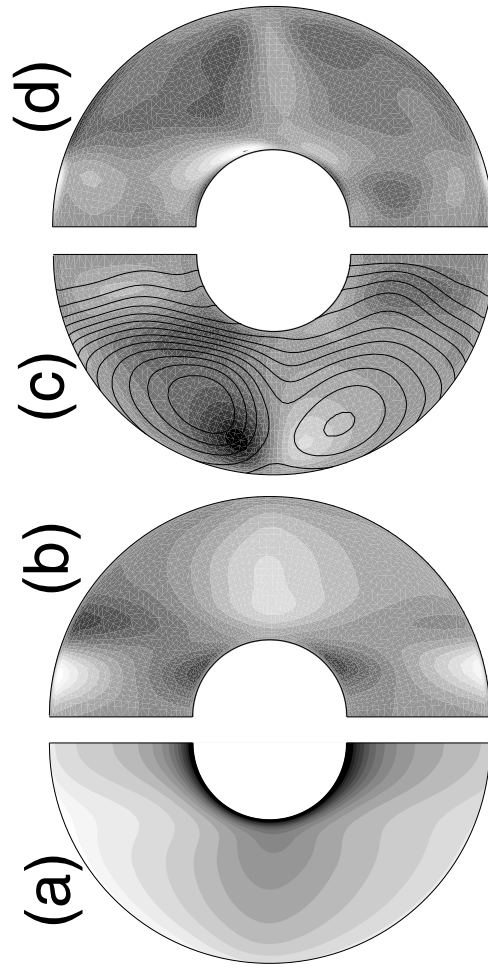


Figure 8. Time-averaged zonal structure of dynamo with Y_{10} boundary heat flow pattern, $q^* = 0.5$, $E = 3 \times 10^{-4}$. (a) Temperature, contour step $1/17$ of mean contrast between inner and outer boundary; (b) azimuthal velocity, contour step 8; (c) poloidal magnetic field lines over azimuthal magnetic field contours, contour interval 0.3; (d) azimuthal electric current. Dark = positive, light = negative.

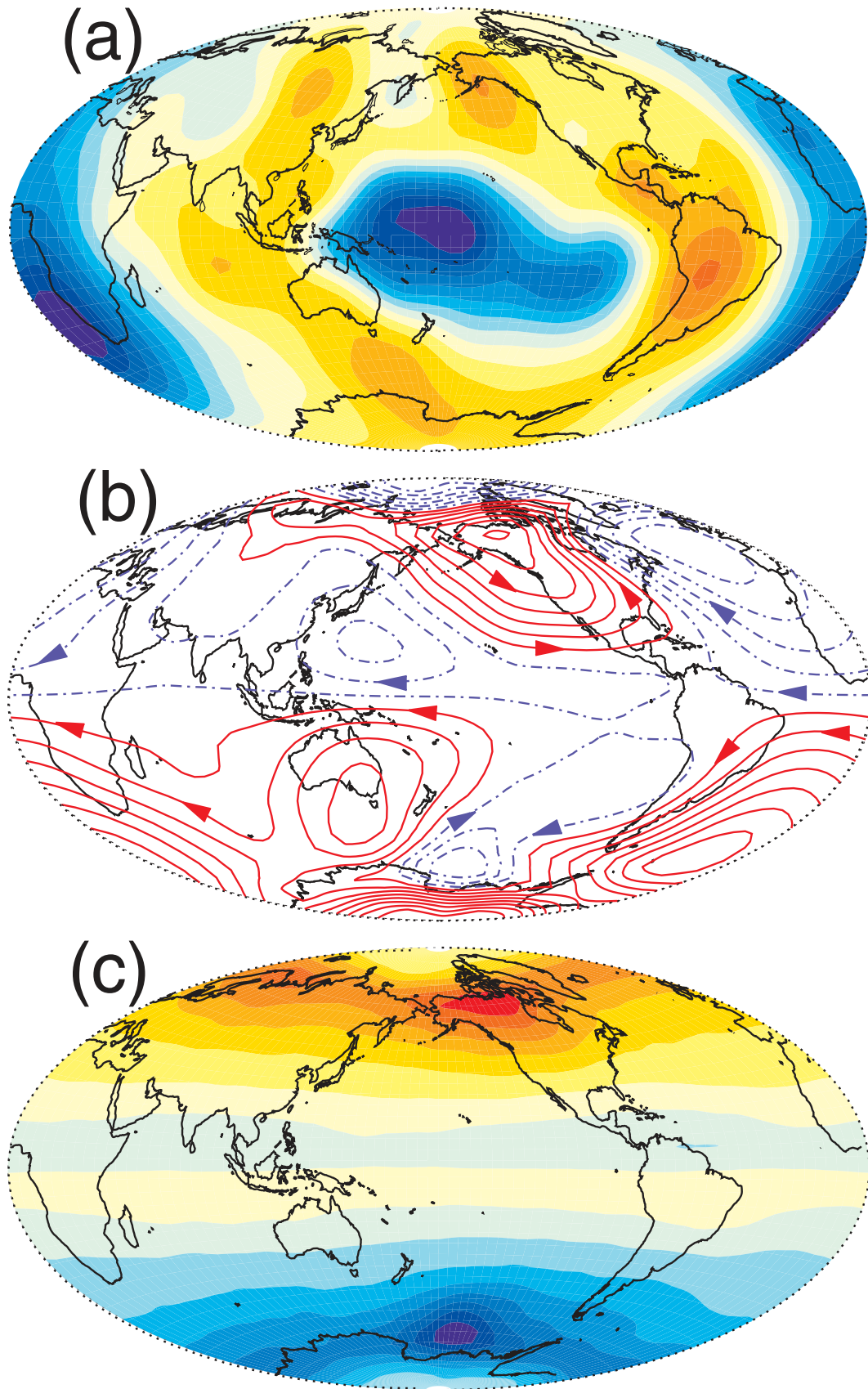


Figure 9. Time-averaged dynamo with tomographic boundary heat flow pattern, $q^* = 0.5$, $E = 3 \times 10^{-4}$. (a) Boundary heat flow heterogeneity; (b) toroidal streamlines (with velocity direction arrows), contour interval 1, at depth $r_0 - r = 0.04$; (c) radial magnetic field at r_0 , contour interval 0.16. Red = positive, blue = negative.

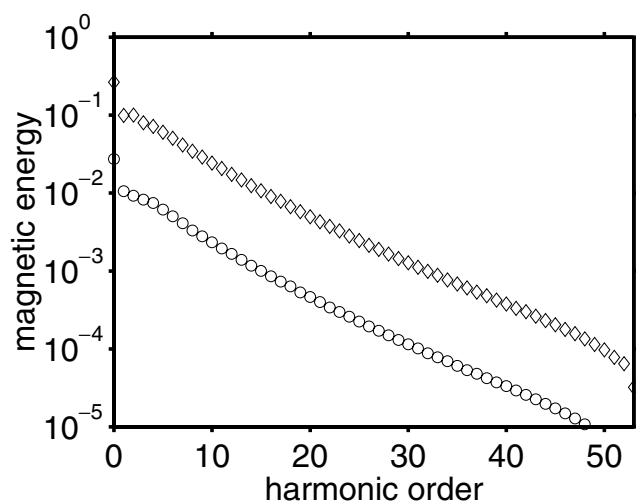


Figure 10. Time average of the magnetic energy versus the harmonic order for uniform (circles) and Y_{22} (diamonds) boundary heat flow cases. The uniform heat flow spectrum is shifted down one decade to avoid overlap.

The tomographic dynamo model in Fig. 9 differs from the historical geomagnetic field on the core–mantle boundary in some aspects. One difference is that the high-intensity magnetic flux patches in the tomographic dynamo model are shifted slightly in longitude and latitude with respect to their locations in the geomagnetic field. For example, the most intense northern hemisphere flux patch in Fig. 9 occurs beneath the western arctic of North America, rather than beneath the northcentral part of North America as it does in the time average of the historical geomagnetic field (Bloxham & Jackson 1992). Similarly, the weaker of the two northern hemisphere patches in Fig. 9 is centred beneath Scandinavia, as opposed to its location beneath central Siberia in the historic geomagnetic field. The patch locations may be biased by the relatively large Ekman number used in this calculation. As shown in Fig. 6, decreasing the Ekman number toward a more realistic value for the core shifts the magnetic flux patches to the east, which would put them closer to their locations in the geomagnetic field. In the southern hemisphere, however, the lone high-intensity flux patch in Fig. 9 is located approximately at the same position as in the time-averaged geomagnetic field (Bloxham & Jackson 1992).

The streamfunction of the toroidal velocity shown in Fig. 9 offers another point of comparison with the geomagnetic field. Models of core flow based on frozen flux inversions of the geomagnetic secular variation (see Bloxham & Jackson 1991, for a review of these) usually include a large-scale anticyclonic gyre in the southern hemisphere, with an equatorward limb located beneath the Indian Ocean and a poleward limb located somewhere beneath South America or the Eastern Pacific, depending on the model. The northern limb of this gyre beneath Africa and the equatorial Atlantic is one of the main expressions of westward drift in the geomagnetic field. Fig. 9 includes an anticyclonic gyre in the southern hemisphere, with a structure quite similar to the southern hemisphere gyre inferred from the geomagnetic secular variation. The transport velocity in the anticyclonic gyre in Fig. 9 is too small by a factor of 10 to explain the westward drift rates in the historical geomagnetic field. However, the dynamo model flow represents an average over nearly 1 Myr, as opposed to the time interval of a few centuries represented in the historical secular variation. In addition, the flow velocity measured by the magnetic Reynolds number is too low in this dynamo model

by a factor of 3 or 4, compared with the core. If the results in Fig. 9 were rescaled to the core using the advection timescale instead of the magnetic diffusion time, the transport velocity of the time-averaged flow would be higher. Another difference between the tomographic dynamo model streamfunction pattern and the flow inferred from the geomagnetic secular variation is the gyre beneath North America. The North American gyre in Fig. 9 is cyclonic, consistent with fluid downwelling and a high magnetic field intensity there. Many core flow maps derived using frozen flux and the geomagnetic secular variation also contain a North American gyre (see Bloxham & Jackson 1991, for examples) but it is usually anticyclonic.

Finally, we point out that the heterogeneous boundary heat flow effects seen in time averages are more difficult to detect in snapshots of the magnetic field. For example, Fig. 10 compares the time average of snapshot magnetic energy spectra for the uniform and Y_{22} boundary heating cases. The energy at spherical harmonic order $m = 2$ is very slightly elevated in the Y_{22} heating case, but the effect is very subtle. Differences in the secular variation among these models are also subtle, and will be considered in a subsequent study.

In comparison with other dynamo models with boundary heat flow heterogeneity, our results are in accord with some of the earlier findings, but also show some differences. We find that the Y_{20} component of the heat flow anomaly controls the relative size of the axial octupole, in agreement with Bloxham (2000b), but in his model a small heat flow anomaly seems to have a larger influence than in our model. Other dynamo models with non-zonal boundary heat flow heterogeneity by Sarson *et al.* (1997), Glatzmaier *et al.* (1999) and Bloxham (2001) find, as we do, high-intensity flux patches in the time-averaged field at high latitudes, although those models show a more direct relationship between the longitude of the flux patches and the longitude of maximum boundary heating than we find. There are parameter differences between those dynamo models and ours, but the biggest difference is that the other three use hyperdiffusivities (that is, scale-dependent functions in place of the diffusion coefficients), whereas we use constant diffusion coefficients. It is known that dynamo models with uniform boundary conditions produce different results with and without hyperdiffusion (Grote *et al.* 2000), and it is expected that these differences will persist with heterogeneous boundary conditions.

6 CONCLUSIONS

The time-averaged structure of the magnetic fields in our numerical dynamos differs substantially from instantaneous, snapshot pictures. Snapshot images of the magnetic field on the outer boundary are dominated by short-wavelength, concentrated magnetic flux patches that are created by the columnar convection. Owing to chaos and longitudinal drift of the convection columns, the short-wavelength part of the magnetic field tends to average toward zero over time.

Uniform boundary heat flow produces an axisymmetric time-averaged magnetic field with hemispherical antisymmetry. The time-averaged field is dipole dominated in this case, but it also includes an octupole component with the same sign as the dipole. In terms of spatial structure, the primary departure from the GAD configuration is found at high latitudes in both hemispheres. It consists of a low-intensity magnetic field directly over the poles, the polar cap minima, and rings of high-intensity field at the latitude of the inner-core tangent cylinder, the tangent cylinder maxima. The polar minima are results of flux divergence by upwelling polar plumes, and the tangent cylinder maxima are results of flux concentration by convergence and downwelling along the tangent cylinder. In terms of spectral components, the largest departure from GAD is the

axial octupole ratio $G30 \simeq +0.06$, which is several times larger than inferred for the 0–5 Ma palaeomagnetic field by Merrill *et al.* (1996), but is comparable to $G30$ estimated for the Palaeozoic field by Kent & Smethurst (1998).

At the other extreme, we find that very strong boundary heterogeneity tends to suppress dynamo action, rather than simply locking the magnetic field to the boundary heterogeneity as some other studies have found. In several cases where the amplitude of the boundary heat flow heterogeneity exceeded the average heat flow, we found dynamo action eventually ceased. Loss of dynamo action through this mechanism would seem to place an upper limit on the amount of heat flow heterogeneity on the core–mantle boundary. However, the effect of heterogeneous heat flow is probably stronger in our models than for the geodynamo. In the core, convection is driven in part by compositional buoyancy derived from crystallization of the inner core, which is not as strongly affected by the boundary heat flow heterogeneity.

We find stable dynamos when the boundary heterogeneity parameter is in the range $-1 < q^* < 1$. To interpret this condition in terms of heat flow on the core–mantle boundary, it is necessary to correct for the effects of compressibility in the core. In our models the fluid is incompressible, so the adiabatic thermal gradient is zero, and there is no difference between the total heat flow and the superadiabatic contribution to the heat flow. In contrast, thermal convection in the core is compressible and is driven by the superadiabatic part of the heat flow. Therefore, q_0 in our models represents the average superadiabatic core heat flow, and the non-uniform heat flow $q'(\theta, \phi)$ in our models represents the deviations of core–mantle boundary heat flow from the average superadiabatic core heat flow.

Most studies of the energetics of the core indicate that the heat conducted down the core adiabat is comparable to the total core heat flow (Lister & Buffett 1995; Labrosse *et al.* 1997). Sumita & Olson (1999) have pointed out how this condition can lead to an unusual situation in the core, in which the heterogeneity parameter q^* can be appreciably large on the core–mantle boundary, even though the absolute heat flow variations q' are relatively small. If the total core–mantle boundary heat flow nearly equals the conduction down the core adiabat, then the average superadiabatic heat flow q_0 is nearly zero there, and according to eq. (1), non-uniform core–mantle boundary heat flow q' results in a large value of the heterogeneity parameter q^* . In this situation the influences of rather small non-uniformities in the actual heat flow on the core–mantle boundary are magnified, producing the relatively large effects on geodynamo we find in our models.

Intermediate amounts of boundary heterogeneity produce a time-averaged magnetic field consisting of an axisymmetric part similar to the field produced with uniform heating, plus an anomalous part directly attributable to the boundary heterogeneity. The amplitude of the anomalous part of the field is proportional to the amplitude of the boundary heat flow heterogeneity. From calculations with single harmonic boundary heating patterns we obtain the following empirical relationship between the anomalous magnetic field and the boundary heat flow pattern: boundary heating at spherical harmonic degree l and order m produces an anomalous field at degree $l + 1$ and order m . Dynamo models with hemispherical differences in boundary heat flow produce departures from GAD with quadrupole field components in the time-averaged magnetic field. A model with elevated heat flow in the northern hemisphere results in positive values of the quadrupole ratio $G20 \simeq +0.07$, larger than the average palaeomagnetic field for 0–5 Ma.

High-density patches of magnetic flux are found in the time-averaged magnetic field in cases with non-axisymmetric bound-

ary heat flow. The patches are formed by the combined action of the axisymmetric tangent cylinder downwelling plus the non-axisymmetric upwellings and downwellings, and are located slightly equatorward from the inner-core tangent cylinder (which is near $\pm 69^\circ$ on the core–mantle boundary). The location of the patches is controlled by the pattern of upwellings and downwellings in the tangent cylinder region. Because downwellings concentrate and upwellings disperse magnetic flux, the high-intensity flux patches are most closely related to the non-axisymmetric downwellings (although not necessarily coincident with them). Equally importantly, the high-intensity flux patches are located away from upwellings. The flux patches are the result of a balance between field line stretching in downwellings and upwellings, and magnetic diffusion. The high-intensity flux patches in our calculations do not occur precisely at the longitudes of either the maximum or the minimum boundary heat flow. Instead the flux patches are shifted westward relative to the boundary heat flow pattern. The amount of westward phase shift depends on the azimuthal wavenumber m , and appears to decrease with decreasing Ekman number. Our calculations do not provide enough information to determine its sensitivity to other factors such as the magnetic field strength.

A dynamo model with a boundary heat flow pattern proportional to the lower-mantle seismic tomography model of Masters *et al.* (1996) truncated at harmonic degree $l = 4$ produces time-averaged magnetic field structures suggestive of the historical average geomagnetic field on the core–mantle boundary. Tomographic boundary heat flow produces a single high-intensity flux patch in the southern hemisphere and an unequal pair of high-intensity flux patches in the northern hemisphere in the time-averaged magnetic field. This model also produces a quadrupole Gauss ratio with the same sign as the time-averaged palaeomagnetic field (although smaller in magnitude), and a pattern of circulation in the southern hemisphere that is similar to the circulation pattern inferred from the historical geomagnetic secular variation.

ACKNOWLEDGMENTS

We especially want to thank the Academy of Sciences in Göttingen for their support of PO as a visiting Gauss Professor at the Institut für Geophysik during the course of this work. UC was supported by a grant from the Deutsche Forschungsgemeinschaft.

REFERENCES

- Bloxham, J., 2000a. The effect of thermal core–mantle interactions on the paleomagnetic secular variation, *Phil. Trans. R. Soc. Lond., A*, **358**, 1171–1179.
- Bloxham, J., 2000b. Sensitivity of the geomagnetic axial dipole to thermal core–mantle interactions, *Nature*, **405**, 63–65.
- Bloxham, J., 2001. High-latitude flux bundles: time-independent and time-dependent behaviour, *2001 IAGA-IASPEI Joint Scientific Assembly Abstracts*, pp. 61–62.
- Bloxham, J. & Gubbins, D., 1987. Thermal core–mantle interactions, *Nature*, **325**, 511–513.
- Bloxham, J. & Jackson, A., 1990. Lateral temperature variations at the core–mantle boundary deduced from the magnetic field, *Geophys. Res. Lett.*, **17**, 1997–2000.
- Bloxham, J. & Jackson, A., 1991. Fluid flow near the surface of Earth's outer core, *Rev. Geophys.*, **29**, 97–120.
- Bloxham, J. & Jackson, A., 1992. Time dependent mapping of the geomagnetic field at the core–mantle boundary, *J. geophys. Res.*, **97**, 19 357–19 564.
- Buffett, B.A., 2000. Earth's core and the geodynamo, *Science*, **288**, 2007–2012.

- Christensen, U., Olson, P. & Glatzmaier, G.A., 1999. Numerical modeling of the geodynamo: a systematic parameter study, *Geophys. J. Int.*, **138**, 393–409.
- Coe, R.S., Hongre, L. & Glatzmaier, G.A., 2000. An examination of simulated geomagnetic reversals from a palaeomagnetic perspective, *Phil. Trans. R. Soc. Lond., A*, **358**, 1141–1170.
- Constable, C.G., Johnson, C.L. & Lund, S.P., 2000. Global geomagnetic field models for the past 3000 years: transient or permanent flux lobes?, *Phil. Trans. R. Soc. Lond., A*, **358**, 991–1008.
- Dormy, E., Valet, J.-P. & Courtillot, V., 2000. Numerical models of the geodynamo and observational constraints, *Geochem. Geophys. Geosys.*, **1**, paper 2000GC000 062.
- Gibbins, S.J. & Gubbins, D., 2000. Convection in the Earth's core driven by lateral variations in the core–mantle boundary heat flux, *Geophys. J. Int.*, **142**, 631–642.
- Glatzmaier, G.A., Coe, R.C., Hongre, L. & Roberts, P.H., 1999. The role of the Earth's mantle in controlling the frequency of geomagnetic reversals, *Nature*, **401**, 885–890.
- Grote, E., Busse, F.H. & Tilgner, A., 2000. Effects of hyperdiffusivities on dynamo simulations, *Geophys. Res. Lett.*, **27**, 2001–2004.
- Gubbins, D. & Bloxham, J., 1987. Morphology of the geomagnetic field and implications for the geodynamo, *Nature*, **325**, 509–511.
- Gubbins, D. & Richards, M., 1986. Coupling of the core dynamo and mantle: thermal or topographic?, *Geophys. Res. Lett.*, **13**, 1521–1524.
- Hide, R., 1970. On the Earth's core–mantle interface, *Q. J. R. Meteorol. Soc.*, **96**, 579–590.
- Jones, G.M., 1977. Thermal interaction of the core and the mantle and long-term behaviour of the geomagnetic field, *J. geophys. Res.*, **82**, 1703–1709.
- Johnson, C.L. & Constable, C.G., 1995. The time averaged geomagnetic field as recorded by lava flows over the past 5 Myr, *Geophys. J. Int.*, **122**, 489–519.
- Johnson, C.L. & Constable, C.G., 1997. The time averaged geomagnetic field: global and regional biases for 0–5 Ma, *Geophys. J. Int.*, **131**, 643–666.
- Kelly, P. & Gubbins, D., 1997. The geomagnetic field over the past 5 million years, *Geophys. J. Int.*, **128**, 315–330.
- Kent, P. & Smethurst, M.H., 1998. Shallow bias of paleomagnetic inclinations in the Paleozoic and Precambrian, *Earth planet. Sci. Lett.*, **160**, 391–402.
- Kono, M., Tanaka, H. & Tsunakawa, H., 2000. Spherical harmonic analysis of paleomagnetic data: the case of linear mapping, *J. geophys. Res.*, **105**, 5817–5833.
- Kutzner, C. & Christensen, U., 2002. From stable dipolar to reversing numerical dynamos, *Phys. Earth planet. Inter.*, in press.
- Labrosse, S., Poirier, J.P. & LeMouél, J.L., 1997. On cooling of the Earth's core, *Phys. Earth planet. Inter.*, **99**, 1–17.
- Lister, J.R. & Buffett, B.A., 1995. The strength and efficiency of thermal and compositional convection in the geodynamo, *Phys. Earth planet. Inter.*, **91**, 17–30.
- Loper, D.E., 1978. Some thermal consequences of the gravitationally powered dynamo, *J. geophys. Res.*, **83**, 5961–5970.
- Masters, G., Johnson, S., Laske, G. & Bolton, H., 1996. A shear-velocity model of the mantle, *Phil. Trans. R. Soc. Lond., A*, **354**, 1385–1411.
- Merrill, R.T., McElhinny, M.W. & McFadden, P.L., 1996. *The Magnetic Field of the Earth: Paleomagnetism, the Core, and the Deep Mantle*, Academic Press, San Diego.
- Moffatt, H.K., 1978. *Magnetic Field Generation in Electrically Conducting Fluids*, Cambridge Univ. Press, Cambridge.
- Olson, P. & Glatzmaier, G.A., 1996. Magnetoconvection and thermal coupling of the Earth's core and mantle, *Phil. Trans. R. Soc. Lond., A*, **354**, 1413–1424.
- Olson, P., Christensen, U. & Glatzmaier, G.A., 1999. Numerical modeling of the geodynamo: mechanisms of field generation and equilibration, *J. geophys. Res.*, **104**, 10 383–10 404.
- Sarson, G.R., Jones, C.A. & Longbottom, A.W., 1997. The influence of boundary region heterogeneities on the geodynamo, *Phys. Earth planet. Inter.*, **101**, 13–32.
- Schubert, G., Turcotte, D.L. & Olson, P., 2001. *Mantle Convection in the Earth and Planets*, Cambridge Univ. Press, Cambridge.
- Secco, R.A. & Schloessin, H.H., 1989. The electrical resistivity of solid and liquid Fe at pressures up to 7 GPa, *J. geophys. Res.*, **94**, 5887–5894.
- Stacey, F., 1992. *Physics of the Earth*, Brookfield Press, Brisbane.
- Sumita, I. & Olson, P., 1999. A Laboratory model for convection in Earth's core driven by a thermally heterogeneous mantle, *Science*, **286**, 1547–1549.
- Sun, Z.-P., Schubert, G. & Glatzmaier, G.A., 1994. Numerical simulations of thermal convection in a rapidly rotating spherical shell cooled inhomogeneously from above, *Geophys. astrophys. Fluid. Dyn.*, **75**, 199–226.
- Wicht, J., 2002. The role of a conducting inner core in numerical dynamo simulations, *Phys. Earth planet. Inter.*, submitted.
- Van der Voo, R. & Torsvik, T., 2001. Long-term late paleozoic and Mesozoic octupole fields, IAGA and IASPEI Joint Scientific Assembly Abstracts, 73.
- Vogt, P.R., 1975. Changes in geomagnetic reversal frequency at times of tectonic change: evidence for coupling between core and upper mantle processes, *Earth planet. Sci. Lett.*, **25**, 313–321.
- Yuen, D.A., Cadek, O., Chopelas, A. & Matyska, C., 1993. Geophysical inferences of thermal-chemical structures in the lower mantle, *Geophys. Res. Lett.*, **20**, 899–902.
- Zhang, K. & Gubbins, D., 1992. On convection in the Earth's core driven by lateral temperature variations in the lower mantle, *Geophys. J. Int.*, **108**, 247–255.
- Zhang, K. & Gubbins, D., 1993. Convection in a rotating spherical fluid shell with an inhomogeneous temperature boundary condition at infinite Prandtl number, *J. Fluid Mech.*, **250**, 209–232.
- Zhang, K. & Gubbins, D., 1996. Convection in a rotating spherical shell with an inhomogeneous temperature boundary condition at finite Prandtl number, *Phys. Fluids*, **8**, 1141–1148.